Acta Biomaterialia 164 (2023) 303–316

Contents lists available at ScienceDirect

Acta Biomaterialia

journal homepage: www.elsevier.com/locate/actbio

Full length article

Non-destructive 3D characterization of the blood vessel wall microstructure in different species and blood vessel types using contrast-enhanced microCT and comparison with synthetic vascular grafts

Lisa Leyssens[a,b], Tim Balcaen[a,b,c], Maïté Pétré[a,b,d], Natalia Béjar Ayllón[a], Walid El Aazmani[b], Alix de Pierpont[a], Grzegorz Pyka[a,b], Valérie Lacroix[e,f], Greet Kerckhofs[a,b,g,h,*]

[a] Mechatronic, Electrical Energy and Dynamic Systems, Institute of Mechanics, Materials, and Civil Engineering, UCLouvain, 1348 Louvain-la-Neuve, Belgium
[b] Pole of Morphology, Institute of Experimental and Clinical Research, UCLouvain, 1200 Woluwe-Saint-Lambert, Belgium
[c] MolDesignS, Sustainable Chemistry for Metals and Molecules, Department of Chemistry, KU Leuven, 3001 Leuven, Belgium
[d] Department BioMechanics, KU Leuven, 3001 Leuven, Belgium
[e] Pole of Cardiovascular Research, Institute of Experimental and Clinical Research, UCLouvain, 1200 Woluwe-Saint-Lambert, Belgium
[f] Cliniques Universitaires Saint-Luc, Service de chirurgie cardiovasculaire et thoracique, 1200 Woluwe-Saint-Lambert, Belgium
[g] Department of Materials Engineering, KU Leuven, 3001 Leuven, Belgium
[h] Prometheus, Division of Skeletal Tissue Engineering, KU Leuven, 3000 Leuven, Belgium

ARTICLE INFO

Article history:
Received 19 December 2022
Revised 14 March 2023
Accepted 7 April 2023
Available online 16 April 2023

Keywords:
Contrast-enhanced X-ray microfocus computed tomography
Microstructure
Blood vessel types
Inter-species differences
Synthetic vascular grafts

ABSTRACT

To improve the current treatment for vascular diseases, such as vascular grafts, intravascular stents, and balloon angioplasty intervention, the evaluation of the native blood vessel microstructure in full 3D could be beneficial. For this purpose, we used contrast-enhanced X-ray microfocus computed tomography (CECT): a combination of X-ray microfocus computed tomography (microCT) and contrast-enhancing staining agents (CESAs) containing high atomic number elements. In this work, we performed a comparative study based on staining time and contrast-enhancement of 2 CESAs: Monolacunary and 1:2 Hafnium-substituted Wells-Dawson polyoxometalate (Mono-WD POM and Hf-WD POM, respectively) for imaging of the porcine aorta. After showing the advantages of Hf-WD POM in terms of contrast enhancement, we expanded our imaging to other species (rat, porcine, and human) and other types of blood vessels (porcine aorta, femoral artery, and vena cava), clearly indicating microstructural differences between different types of blood vessels and different species. We then showed the possibility to extract useful 3D quantitative information from the rat and porcine aortic wall, potentially to be used for computational modeling or for future design optimization of graft materials. Finally, a structural comparison with existing synthetic vascular grafts was made. This information will allow to better understand the *in vivo* functioning of native blood vessels and to improve the current disease treatments.

Statement of significance

Synthetic vascular grafts, used as treatment for some cardiovascular diseases, still often fail clinically, potentially because of a mismatch in mechanical behaviour between the native blood vessel and the graft. To better understand the causes of this mismatch, we studied the full 3D microstructure of blood vessels. For this, we identified Hafnium-substituted Wells-Dawson polyoxometalate as contrast-enhancing staining agent to perform contrast-enhanced X-ray microfocus computed tomography. This technique allowed to show important differences in the microstructure of different types of blood vessels and in different species, as well as with that of synthetic grafts. This information can lead to a better understanding of the functioning of blood vessels and will allow to improve current disease treatments, such as vascular grafts.

© 2023 Acta Materialia Inc. Published by Elsevier Ltd. All rights reserved.

Abbreviations: CECT, contrast-enhanced X-ray microfocus computed tomography; CESA, contrast-enhancing staining agent; Hf-WD POM, 1:2 Hafnium-substituted Wells-Dawson polyoxometalate; Mono-WD POM, monolacunary Wells-Dawson polyoxometalate; SMC, smooth muscle cell.

* Corresponding author at: Mechatronic, Electrical Energy and Dynamic Systems, Institute of Mechanics, Materials, and Civil Engineering, UCLouvain, Place du Levant 2, 1348 Louvain-la-Neuve, Belgium.

E-mail address: greet.kerckhofs@uclouvain.be (G. Kerckhofs).

https://doi.org/10.1016/j.actbio.2023.04.013
1742-7061/© 2023 Acta Materialia Inc. Published by Elsevier Ltd. All rights reserved.

1. Introduction

Vascular diseases are a major cause of death and disability. The most common forms of diseases of the arteries include atherosclerosis [1,2], aneurysm [3,4], stiffening of the wall due to ageing [5,6], and dissection [7–9]. Venous diseases, such as chronic venous insufficiency and varicose veins, are also prevalent [10–12], causing venous wall injuries and inflammation with significant physical and psychological impact. To treat complications, proper surgical actions must be undertaken. In the case of vessel calcification and occlusion, one of the most common vascular pathologies, different options exist, such as bypass surgery. Bypasses are made using autologous vessels or prosthetic vascular conduits also known as vascular grafts. For the latter, elastic polymers have often been used with the aim of matching the elastic behavior of the host arteries. Although polymer-based synthetic bypass grafts, such as Dacron [13–16] and Gore-Tex [17,18], are clinically used, complications that affect their performance still remain, such as mechanical failure and progressive dilation [19–21]. It is often hypothesized that this is due to a mismatch in compliance between the graft and the native vessel and due to biocompatibility issues [22–26].

Another potential reason for clinical complication is that animal models are often used to study cardiovascular diseases and their treatments. However, the microstructure and composition of the blood vessels might vary from one species to the other. Through classical 2D histological studies, structural differences have already been observed between human and porcine aortic tissues [27]. Moreover, disease treatments are often not adapted from one blood vessel type to the other. Structural differences between the porcine aorta and vena cava have been studied through classical 2D histology and multiphoton imaging, showing important differences in elastin and collagen content and orientation of these fibers, leading to differences in mechanical properties [28]. For the study of vascular diseases or disease treatment options, differences in vessel microstructure should be considered.

For better understanding and treating vascular diseases or for obtaining better tissue models, there is a need to better characterize the microstructure and mechanical properties of diseased tissues [29,30] but also to visualize and quantify the structural properties of healthy tissue in 3D at high resolution on *ex vivo* harvested samples. This could lead to a better understanding of the link between microstructure and proper functioning of the vessel and of the influence of disease on the microstructure and this information is important to improve the design of vascular grafts.

Blood vessels are typically described as being composed of three main layers: the tunica intima (single layer of endothelial cells), the tunica media (contains mainly elastic lamellae, collagen fibers, and smooth muscle cells (SMCs)), and the tunica adventitia (composed mainly of fibrous connective tissue, such as collagen fibers). Different types of arteries can be distinguished. The largest arteries in the body are highly elastic, as they contain a lot of elastin and collagen in their tunica media conferring them pulse-smoothing properties. The medium-sized vessels or muscular arteries have a larger quantity of SMCs to contract and expand in order to supply blood to the peripheral system. Veins and venules are thinner and are composed of lower amounts of SMCs and elastin, since they transport low-pressure blood [31].

2D histological sectioning techniques are still the gold standard for microscopical tissue visualization, but they are not well suited for 3D visualization. Scanning electron microscopy [32,33], confocal laser microscopy [34,35], and multiphoton microscopy [28,36] have shown their potential to produce high-resolution, 3D images, but they only allow visualization of small tissue volumes. Light sheet fluorescence microscopy allows fast imaging of larger tissues but at lower resolution [37–39]. X-ray microfocus computed tomography (microCT) has proven to provide high-resolution, 3D microstructural information of larger and complex materials. To visualize the different soft tissue constituents in the vessel wall, synchrotron phase-enhancement is often required [40–43]. However, access to synchrotron equipment is limited and costly. Lab-based absorption microCT is more readily available and can be used to visualize the different low X-ray-attenuating soft tissues using contrast-enhancing staining agents (CESAs). This technique is then referred to contrast-enhanced microCT (CECT). CECT has been applied for imaging vascular tissues, but many limitations are still present today in terms of spatial resolution and the invasive character of the CESAs being used [44]. *Butters et al.* [45] and *Balint et al.* [46] have investigated the diffusion kinetics of different CESAs in biological tissues, such as Lugol's iodine solution (I_2KI), phosphotungstic acid (PTA), and phosphomolybdic acid (PMA). These CESAs are commonly used for CECT of the cardiovascular system [47–50]. However, they have shown to be destructive [50–53]. Iodine will participate in multiple chemical reactions with the tissue, and as a consequence of these reaction mechanisms, protons are released in the solution acidifying the staining solution [53]. PTA and PMA are considered very acidic compounds [53] and will harm the tissue by inducing extensive tissue shrinkage, resulting in an altered microstructure. In previous studies, our group has shown the potential of Monolacunary and 1:2 Hafnium-substituted Wells-Dawson polyoxometalates (Mono-WD POM and Hf-WD POM, respectively) for non-destructive staining of kidney and soft skeletal tissues [54,55]. Mono-WD POM and Hf-WD POM are synthesized as the salt of the acid and, hence they are not acidifying the solution, causing less tissue shrinkage. However, these POMs have never been used for imaging blood vessels. In this study, we assessed the penetration rate and the contrast-enhancement in the porcine aorta by Mono-WD POM and Hf-WD POM. Providing superior contrast-enhancement, Hf-WD POM was used as CESA for the remainder of the experiments, in which a comparison was made between different species (rat, porcine, and human) for two vessel types (aorta and femoral artery) and between different porcine vessel types (aorta, femoral artery, and vena cava). We additionally quantified the 3D thickness of the different vessel layers as well as different structural parameters of the elastic lamellae in the porcine aorta. We showed the potential of CECT to image an atherosclerotic human femoral artery. Finally, we performed a structural characterization of different currently clinically used synthetic vascular grafts to assess their differences with native tissue.

2. Materials and methods

2.1. Animal age, sex and origin

Porcine aortas were obtained from the slaughterhouse (RIMA Vleesgroothandel, Mechelen, Belgium and WestVlees, Staden, Belgium). The rat aortas and femoral arteries were gathered from waste material from a study at the CARD department (UCLouvain) approved by local authorities (Comité d'éthique facultaire pour l'expérimentation animale, 2016/UCL/MD/027 and 2021/UCL/MD/012) and performed in accordance with the Guide for the Care and Use of Laboratory Animals, published by the US National Institutes of Health (NIH Publication, revised 2011). The human aortas were remaining material from body donations (UCLouvain Biothèque, notification number BB190051). The porcine femoral arteries were obtained from Landrace pigs autopsied during ongoing experiments at the Department of Cardiac Surgery of KU Leuven (ECD 026/2019). The human femoral arteries were donated by the European Homograft Bank (donor bank). An end-stage atherosclerotic human femoral artery was obtained from an amputated patient (EC Research S number: S62776).

2.2. Preparation of the blood vessels

For each type of healthy blood vessel, only three samples were harvested, due to time constraints and limited sample availability. All the biological tissues were fixed using 4% formaldehyde (FA) in phosphate-buffered saline (10 mM, pH = 7.4) (PBS), for 48 h at 4 °C on a shaker plate to improve CESA diffusion. The porcine and human aortas and the porcine vena cavas were cut in square-shaped samples of 1 × 1 cm. The orientation of the samples (circumferential vs. axial direction, luminal vs. adventitial side, proximal vs. distal side) was referenced by cutting a small triangle from the upper right corner of each piece of tissue. For the rat aortas and the rat, porcine, and human femoral arteries (healthy and diseased), the entire circumference of the sample was kept and a piece of 0.5 cm (rat femoral artery) or 1 cm (for all the others) in length was used. For the *CECT and classical 2D histology comparison* study, a smaller piece of porcine aorta of 0.5 × 0.8 cm was cut. For the different aortas, the samples were always dissected from the descending thoracic aorta.

2.3. Contrast-enhancing staining agents

The Monolacunary Wells-Dawson POM α_2-$K_{10}P_2W_{17}O_{61}\bullet 20H_2O$ (α_2-P_2W_{17} or Mono-WD POM) and 1:2 Hafnium(IV)-substituted Wells-Dawson POM $K_{16}[Hf(\alpha_2\text{-}P_2W_{17}O_{61})_2]\bullet 19H_2O$ (α_2-HfP_2W_{17} or Hf-WD POM) were synthesized as described in literature [56,57]. For the *penetration rate and contrast-enhancement* study, samples were stained either with Mono-WD POM or with Hf-WD POM. For all the other studies, Hf-WD POM was used. Staining solutions (pH = 7.32) were prepared by dissolving 35.0 mg/mL (3.5%) POM in PBS. For the Mono-WD POM, 3 mg/mL of lithium chloride (LiCl) was added as previously described [54,58]. Samples were immersed in separate tubes, containing 5 mL of staining solution each. This ensured that the volume of CESA solution was at least 20 times the volume of the samples. Staining time was different for all the samples depending on their size. For the *penetration rate* study, different staining times were applied (0, 3, 6, 9, 24, 48, 72, 168, 240, 360 h). For the *contrast-enhancement* study, porcine aortas were stained 15 days with Hf-WD POM and 48 h with Mono-WD POM + LiCl. For the *CECT and classical 2D histology comparison,* the porcine aorta was stained 7 days. The rat aortas, rat femoral arteries, and porcine vena cavas were stained for 48 h. The porcine and human femoral arteries (healthy and diseased) were stained for 7 days. The human aortas were stained for 12 days. Biological samples were removed from their staining solution and wrapped in parafilm in their wet state to avoid dehydration or degradation during acquisition. They were placed and attached in a dedicated sample holder to avoid any movement during CECT acquisition.

2.4. Synthetic grafts

Three different synthetic grafts were purchased: Dacron (DuPont, USA), Gore-Tex (Gore, USA), and Vectra (Thoratec laboratories corporation, USA). Dacron (polyethylene terephthalate, PET) and GoreTex (expanded polytetrafluoroethylene, ePTFE) are used in a surgical procedure to bypass a diseased blood vessel, while Vectra (three-layered polyetherurethaneurea with non-porous layer under the luminal surface) is a specialty graft for creating vascular access in hemodialysis [59]. The grafts were cut in square-shaped pieces of 1 × 1 cm. The synthetic grafts were not stained, they were placed and attached in a dedicated sample holder to avoid movement during microCT acquisition.

2.5. High-resolution microCT imaging

MicroCT datasets were acquired using a Phoenix NanoTom M (GE Measurement and Control Solutions, Germany) equipped with a 180-kV/15W energy micro/nanofocus X-ray tube. The detector area is 2400 × 3072 pixels (height x width). A diamond-coated tungsten target was used for all scans. The biological samples were stained with a CESA and then imaged with microCT (referred to as CECT). The synthetic grafts were imaged with microCT (no staining). An overview of the microCT and CECT acquisition parameters is given in Table 1. The expected resolution is two to three time the voxel size [60]. The microCT and CECT datasets were reconstructed with the Datos|x software (GE Measurement and Control Solutions) and exported as XY slices (.tiff). A beam hardening correction (BHC) of 6 was applied for biological tissues and 7 for the synthetic graft materials. BHC goes on a scale from 0 (no correction applied) to 10 (very strong correction applied). Three different filters were applied: inline median (projections are filtered during reconstruction using a 3 × 3 median filter which reduces the noise in the volume), ROI-CT (increases the resolution of the CT dataset for a selected ROI of the object), and filter volume (volume is filtered in slices after reconstruction using the Unsharp Masking Filter). For the *penetration rate and contrast-enhancement* study, samples were imaged together with a reference material (aluminum oxide bead (Al_2O_3)) for gray value normalization. In all the other cases, the reference materials were air and parafilm.

2.6. Classical 2D histological assessment

One previously CESA-stained and CECT-imaged biological sample of each kind was washed in PBS for at least 1 day to remove residual staining solution of the surface of the sample and was then embedded in paraffin. The embedding protocol goes as follows: samples were placed in successive baths: formalin solution (37 °C, 45 min), ethanol 70% (37 °C, 30 min), ethanol 90% (37 °C, 45 min), isopropyl alcohol (4 baths, 37 °C, 30 min, 45 min, 1 h, 1 h), toluene (3 baths, 37 °C, 45 min, 1 h, 1 h), paraffin (4 baths, 58 °C, 30 min, 1 h, 1 h, 1 h). Samples were then embedded in paraffin in a cassette and cooled down for the paraffin to harden. Sections with a thickness of 5 µm were cut using a microtome and stained with Verhoeff's stain. Histological sections were imaged using a SNC400 Slice Scanner (Leica Microsystems, Germany).

2.7. Image processing and analysis

For each acquired dataset, an in-house developed Matlab (Mathworks, Natick, USA) script was used to convert the 16-bit-slices (.tiff) to 8-bit slices (.bmp), while simultaneously adapting the grayscale histograms of the datasets to normalize them to each other [55,61]. Then, all the datasets were segmented using the Magic Wand and Watershed segmentation tools in the Avizo software (Thermo Fischer Scientific, Massachusetts, USA) to remove the background. All 3D renderings were generated in Avizo.

2.8. Statistical analysis

GraphPad Prism 9 (GraphPad Software, California, USA) was used for the statistical analysis and data visualization. Normality and homoscedasticity of the residuals were checked before doing each statistical test. To ensure that normality and homoscedasticity were met, a logarithmic (Log10) transformation of the data was sometimes necessary. When a comparison was made between two groups, a two-sided *t*-test was performed. The Welch's correction was applied in case of unequal variances. A nonparametric

Table 1
MicroCT and CECT acquisition parameters for all types of samples.

	Porcine aorta (Fig. 1A-D)	Porcine aorta (Fig. 1E-F, Fig. 3, Fig. 4, Fig. 5, suppl. Video 1)	Porcine aorta (Fig. 2)	Rat aorta (Fig. 3 and Fig. 5)	Human aorta (Fig. 3)	Porcine femoral artery (Suppl. Fig. 1, Fig. 4, suppl. Video 1)	Rat femoral artery (Suppl. Fig. 1)	Human femoral artery (Suppl. Fig. 1)	Porcine vena cava (Fig. 4, suppl. Video 1)	Atherosclerotic human femoral artery (Video 1)	Synthetic grafts (Fig. 6)
Isotropic voxel size (µm)	8.6	2.75–2.8	4/1.68	1.12	1.5–2	1.75–2.5	1	2.72–3.11	2.75	2.5	3
Source voltage (kV)	80	70	60/90	70	70	80	70	60–80	80	120	50
Tube current (µA)	450	168	281/78	60	90–120	90	60	160–190	140	80	250
Exposure time (ms)	500	750	500	500	500	500	500	500	500	500	500
Mode	0	0	0	0	0	0	0	0	0	0	0
Number of images	1800	2400	2400	2400	2400	2400	2400	2400	2400	2400	2400
Average	1	3	1/3	3	2-3	3	2	1	1	3	1
Skip	0	1	0/1	1	1	1	1	0	0	1	0
Fast scan mode	YES	NO	YES/NO	NO	NO	NO	NO	YES	YES	NO	YES
Scan time (min)	15	129	34/86	89	60–129	89	69	20	20	86	20

test was performed in case the distribution was not normal. When more than two groups were compared, a one-way ANOVA was applied, followed by a Tukey's multiple comparisons test. Welch's correction was applied in case of unequal variances, followed by a Dunnett's T3 multiples comparisons test. A mixed-effects analysis was performed when $n = 3$ with repeated measures, followed by a Bonferroni's multiple comparisons test. The Geisser-Greenhouse correction was applied in case of unequal variances, followed by a Tukey's multiple comparisons test. *P*-values below 0.05 were considered to be significant; ns $p > 0.05$, * $p \leq 0.05$, ** $p \leq 0.01$, *** $p \leq 0.001$, **** $p \leq 0.0001$. For the distribution graphs (Fig. 5), *p*-values were calculated based on the difference between the mean of the distributions. All the statistical tests were verified after consultation with a statistician. In the bar graphs, the mean value of the different samples is indicated by the height of the bars and individual values are also represented. Error bars represent the standard deviation.

A) **Penetration rate and contrast-enhancement study.**

The datasets of the same samples (number of samples (n) = 2 for both Mono-WD POM and Hf-WD POM) but different time points were registered to each other (Avizo registration wizard). A volume of interest (VOI) of 400 slices was selected for each dataset. One registered slice from each dataset for each time point was then selected and the grayscale values along a line through the sample were computed using Dataviewer (Bruker Micro-CT, Kontich, Belgium). As the adventitia (loose connective tissue) has a variable thickness and is stained rapidly (fully stained after 3 h for all samples), it was not considered in the grayscale value measurements. A point at $x = 0$ mm was defined at the location where the tunica media starts (on the side of the adventitia). The remaining segment was discretized into smaller segments of 86 µm (10 pixels). The gray value for each small segment was the mean value of all the values from the segment. The grayscale for three different locations inside the tissue was stored: 14.5 pixels (0.0985 mm approximated to 0.1 mm), 44.5 pixels (0.3025 mm ~ 0.3 mm), and 74.5 pixels (0.5066 mm ~ 0.5 mm). The experimental data was fit to an exponential plateau equation (Eq. 1.).

$$I = I_{\max} - (I_{\max} - I_0)e^{(-kt)} \quad (1)$$

where I_0 is the mean of all gray values at t = 0, I_{max} is the mean gray value at the latest time point, and k is found by minimizing the sum of squared values between the curve and the experimental data. Finally, a saturation level of $\frac{I}{I_{max}} = 99\%$ was defined, which allowed to compute the staining time necessary for each position inside the tissue. This data was fit to an exponential equation (Eq. 2.)

$$t = Ae^{cx} \quad (2)$$

where t is the staining time, x is the location inside the tissue and A and c are constants that have been fitted to minimize the sum of squared values between the curve and the experimental data.

On high-resolution CECT images of smaller pieces of porcine aorta ($n = 3$), the contrast difference between the elastic lamellae and the background (mainly collagen and SMCs) was determined by calculating the grayscale difference between peaks and valleys of grayscale lines drawn perpendicular to the orientation of the elastic lamellae on 2D slices (in-house developed Python code). Three lines were drawn on 16 slices for each dataset ($n = 3$ per condition).

B) **CECT and paraffin embedding: volume comparison study.**

Three fresh pieces of porcine aorta were imaged at low resolution (4 µm voxel size), then fixed in 4% FA and imaged again at low resolution (4 µm). The pieces were stained in Hf-WD POM and imaged at low resolution (4 µm) and high resolution (1.68 µm). They were then embedded in paraffin and imaged again at low (4 µm) and high resolution (1.68 µm). The low-resolution imaging allowed to visualize the entire samples and compute their volume to make a comparison between fresh, fixed, stained, and embedded tissue volumes. The high-resolution datasets only allowed to visualize a small VOI in the sample and were registered to each other to allow a one-on-one visual comparison between stained and embedded tissue ($n = 3$).

C) **Inter-species differences study.**

For the three types of aortas and the three types of femoral arteries, the adventitia and the media were segmented from each other using the Avizo software (Magic Wand and Watershed segmentation tools). The thickness distribution of each layer (media and adventitia) was computed using the 3D analysis in CTAn (Bruker MicroCT, Kontich, Belgium), which uses a sphere-fitting algorithm [62] on binarized images. We chose to remove all thicknesses below 1% in the frequency thickness distribution. The mean and standard deviation of the thickness of the media and the adventitia were then computed for all samples and normalized to the full vessel thickness. Thickness of the media and adventitia were compared between each other for each vessel type. The full thickness of each vessel was also computed and compared between species ($n = 3$ per sample type).

D) **Comparison study between different types of blood vessels.**

Avizo was used to generate a video comparing the microstructure of the porcine aorta, femoral artery, and vena cava in 3D. The thickness of the media and adventitia of the vena cava were computed in 3D with CTAn in the same way as for the femoral arteries and the aortas. For each type of porcine blood vessel (aorta, femoral artery, and vena cava), the thickness of each layer was normalized to the thickness of the entire wall and was plotted to compare the relative thickness of each layer ($n = 3$ per sample type).

E) **Quantification of different structural parameters in different types of blood vessels.**

In the rat and in the porcine aortas, three VOIs of 250 × 54 × 60 pixels (approximately 280 × 60 × 67 µm) and 150 × 150 × 150 pixels (420 × 420 × 420 µm), respectively, were selected on each side (intima and adventitia) of the medial layer of each aorta ($n = 3$ samples). Each VOI was filtered using the following filters, available in Avizo: median filter (interpretation 3D, neighborhood 6, iterations 3), deblur (sharpening factor 5), median filter (interpretation 3D, neighborhood 6, iterations 3), deblur (sharpening factor 5), and Gaussian filter (interpretation 3D, kernel type separable, standard deviation 1, kernel size factor 2). The elastic lamellae were segmented using the Magic Wand tool (Avizo). The following parameters were computed for the elastic lamellae using the 3D thickness analysis (CTAn): thickness distribution (µm), separation (or distance between elastic lamellae) distribution (µm), and connectivity density (connectivity, determined by calculating the Euler characteristic, divided by sample volume in μm^{-3} [63]). The volume fraction (volume of elastic lamellae over total VOI volume) and the tortuosity of the elastic lamellae inside a VOI were computed using Tau factor, a Matlab tool developed by Cooper et al. [55]. The tortuosity factor τ is computed by calculating the reduction in diffusive transport caused by convolution in the geometry of heterogeneous media (Eq. 3.).

$$D^{eff} = D\frac{\epsilon}{\tau} \tag{3}$$

where ϵ is the volume fraction of the conductive phase; D is the intrinsic diffusivity of the conductive phase; and D^{eff} is the effective diffusivity through a porous volume where the second phase is insulating.

F) **Comparison between healthy and atherosclerotic human femoral artery: imaging and segmentation**

The different tissue constituents of an atherosclerotic human femoral artery were segmented with Avizo using the magic wand and watershed segmentation tools. A video was generated in Avizo to compare the healthy and the atherosclerotic human femoral arteries.

G) **Structural analysis of the synthetic grafts.**

For the evaluation of the structural parameters (fiber thickness, fiber separation, and fiber volume fraction), images were filtered (Gaussian filter, 3D space, squared kernel with radius 3) and binarized using manual thresholding, and structural parameters were computed with the 3D analysis tool (CTAn) ($n = 5$ for Dacron and $n = 6$ for Gore-Tex and Vectra). The fiber thickness is the average thickness of the material present between the pores (µm). The fiber separation is the average size of the pores (µm). The volume fraction in the volume of the object (fibers) divided by the total volume of the graft (%).

3. Results

3.1. Screening of CESAs based on penetration rate and contrast-enhancement

To select the optimal CESA for blood vessel staining and the visualization of the blood vessel wall microstructure, the penetration rate and contrast-enhancement of both Mono-WD POM and Hf-WD POM were compared using porcine aorta samples. Visual comparison showed that the penetration is faster for Mono-WD POM than for Hf-WD POM (Fig. 1A). After 48 h, the tissue was fully stained with Mono-WD POM, while it was only fully stained with Hf-WD POM after 15 days (Fig. 1B-D). Hf-WD POM staining resulted in a higher final gray value than Mono-WD POM staining, confirmed by the different plateau level of the normalized gray value. High resolution images (2.75–2.8 µm voxel size) were then used to compare the microstructure of the same tissue with both CESAs (Fig. 1E–F). From these images, we assume more POM is present in the elastic lamellae when staining with Hf-WD POM compared to Mono-WD POM (Fig. 1E–F). This was confirmed by measuring the difference in contrast between the elastin sheets and the background for both CESAs (Fig. 1H). Classical 2D histological sections colored with Verhoeff's stain confirmed that the bright areas in the CECT images are the elastic lamellae (Fig. 1G). Because of the higher contrast between the elastic lamellae and the background (*i.e.* SMCs and collagen) for Hf-WD POM staining compared to Mono-WD POM, this CESA was selected for the remainder of the experiments, despite its slower penetration through the tissue.

3.2. Sample preparation for classical 2D histology causes tissue deformation

Classical 2D histology is still the reference in the field and is often used to validate CECT-based acquired images. To evaluate the influence of sample preparation and image acquisition of both techniques on tissue integrity, the volumes of different pieces of porcine aorta were computed at different stages of the sample preparation (Fig. 2). The fixation of the tissue in 4%FA induced a shrinkage of 18.5% ± 4.0% compared to the fresh state (Fig. 2B), while the staining with Hf-WD POM caused an increase in volume of 17.9% ± 3.9% (Fig. 2C) compared to the fixed state. Subsequent embedding in paraffin for classical 2D histology caused a decrease in volume of the tissue of 45.3± 3.1% compared to the fresh state and of 43.0% ± 3.1% compared to the stained state (Fig. 2D). It shows that validation of CECT using classical 2D histological sections is possible only in a visual manner but not quantitatively.

3.3. Important differences in microstructure between the rat, porcine and human aorta and femoral artery

The difficulty in obtaining human tissue often leads to the use of animal models, which are then extrapolated to humans. However, differences between species are an important factor to consider when studying diseases or treatment options. Here, rat, porcine, and human aortas and femoral arteries were compared visually and using layer thickness measurements to show the differences in microstructure and size of the arteries among these species (Fig. 3 and Suppl. Fig. 1). For all species, there is a heterogeneous arrangement of the elastic lamellae present in the medial layer of the aorta, although this is much less present for the rat aorta (Fig. 3A). Close to the intima, the sheets are less densely packed and more wavy while close to the adventitia, the sheets are densely packed to each other and less wavy. The porcine and human aorta have a similar thickness, while the rat aorta is significantly thinner than both. However, the normalized thickness of the adventitia and the media compared to the full vessel thickness

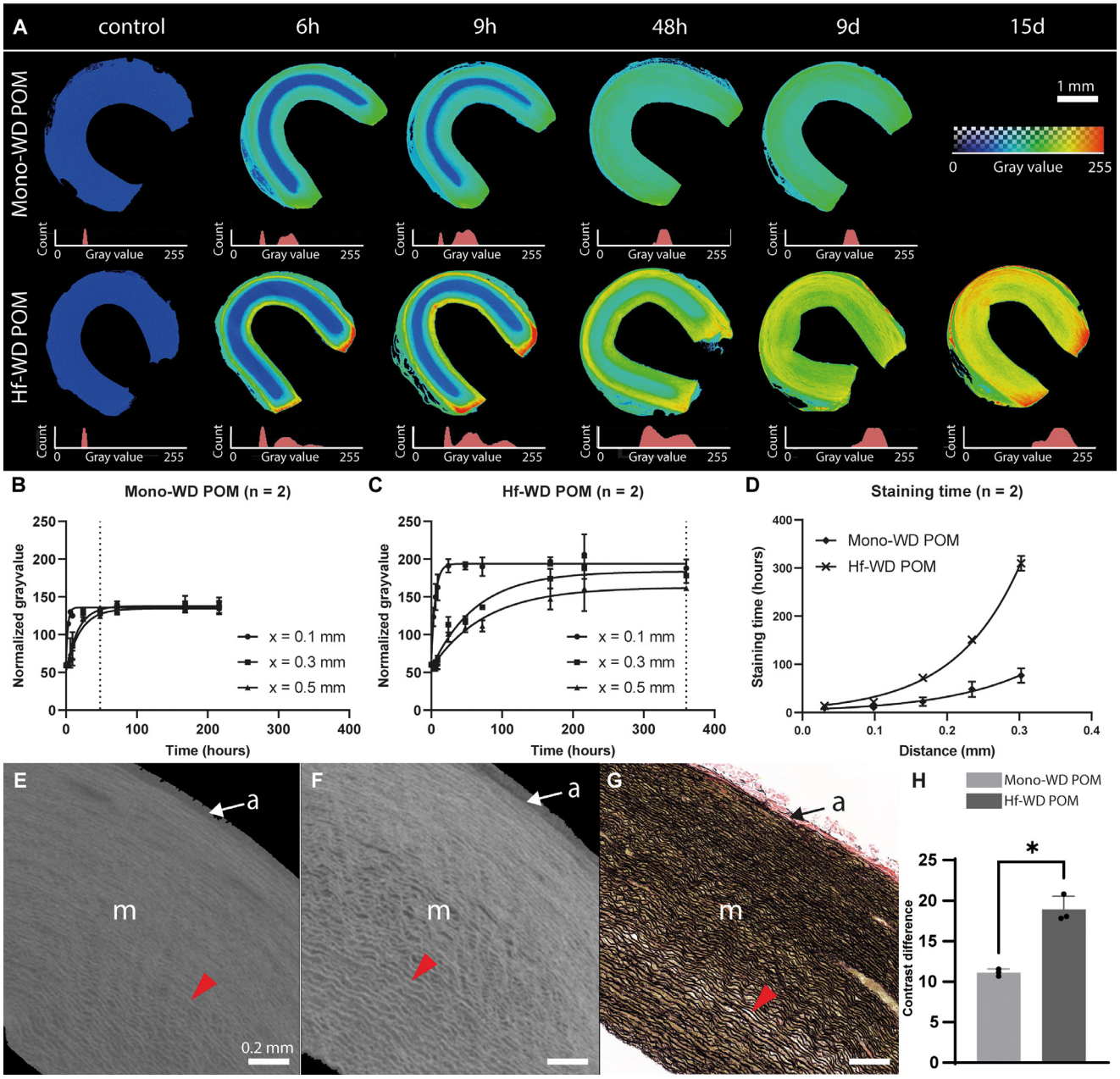


Fig. 1. CESA staining in function of time: Mono-WD POM and Hf-WD POM. (A) CECT-based cross-sections for a few selected time points, the color-legend scalebar goes from 0 to 255 of gray values and the gray value histogram is shown below in red. (B-C) Normalized gray value in function of time for different locations (x) inside the tissue and fitted with an exponential decay curve for (B) Mono-WD POM and (C) Hf-WD POM. Dotted vertical line represents full staining of the tissue. (D) Staining time needed for the CESA to reach a certain distance inside the tissue. Comparison of high-resolution CECT-based cross-section of porcine aorta stained with (E) Mono-WD POM and (F) Hf-WD POM and comparison with (G) classical 2D histological analysis with Verhoeff's stain, a = adventitia, m = media, red arrowhead = elastic lamella. (H) Contrast difference between elastic lamellae and background (SMCs and collagen) for Mono-WD POM and Hf-WD POM-stained samples. Scalebar = 1 mm for (A) and 0.2 mm for (E-G), number of samples (n) = 2 (B-D) and n = 3 (H), * $p \leq 0.05$. (For interpretation of the references to color in this figure legend, the reader is referred to the web version of this article.)

is similar for all species. The media is the thickest layer with approximately 82% of full vessel thickness on average for all species (Fig. 3B). Contrary to the aorta, for the femoral artery, there are clear visual differences in microstructure between the porcine and human samples (Suppl. Fig. 1). In the porcine femoral artery, the external elastic lamina (EEL) is a thick layer of connected sheets (~131 μm) and we defined it to be part of the media where most of the elastin is located. In the human and rat femoral arteries, the EEL is composed of only one (rat) or a few (human) elastic lamellae. The variation in full vessel thickness between all three species is larger for the femoral artery with an increasing thickness going from rat (average thickness = 81.48 μm) to porcine (average thickness = 671.37 μm) to human (average thickness = 1328.73 μm). The difference in normalized thickness between media and adventitia is highly variable among species. The average media thickness is 47.97%, 85.88%, and 69.60% of full vessel thickness for the rat, porcine, and human femoral artery, respectively (Suppl. Fig. 1).

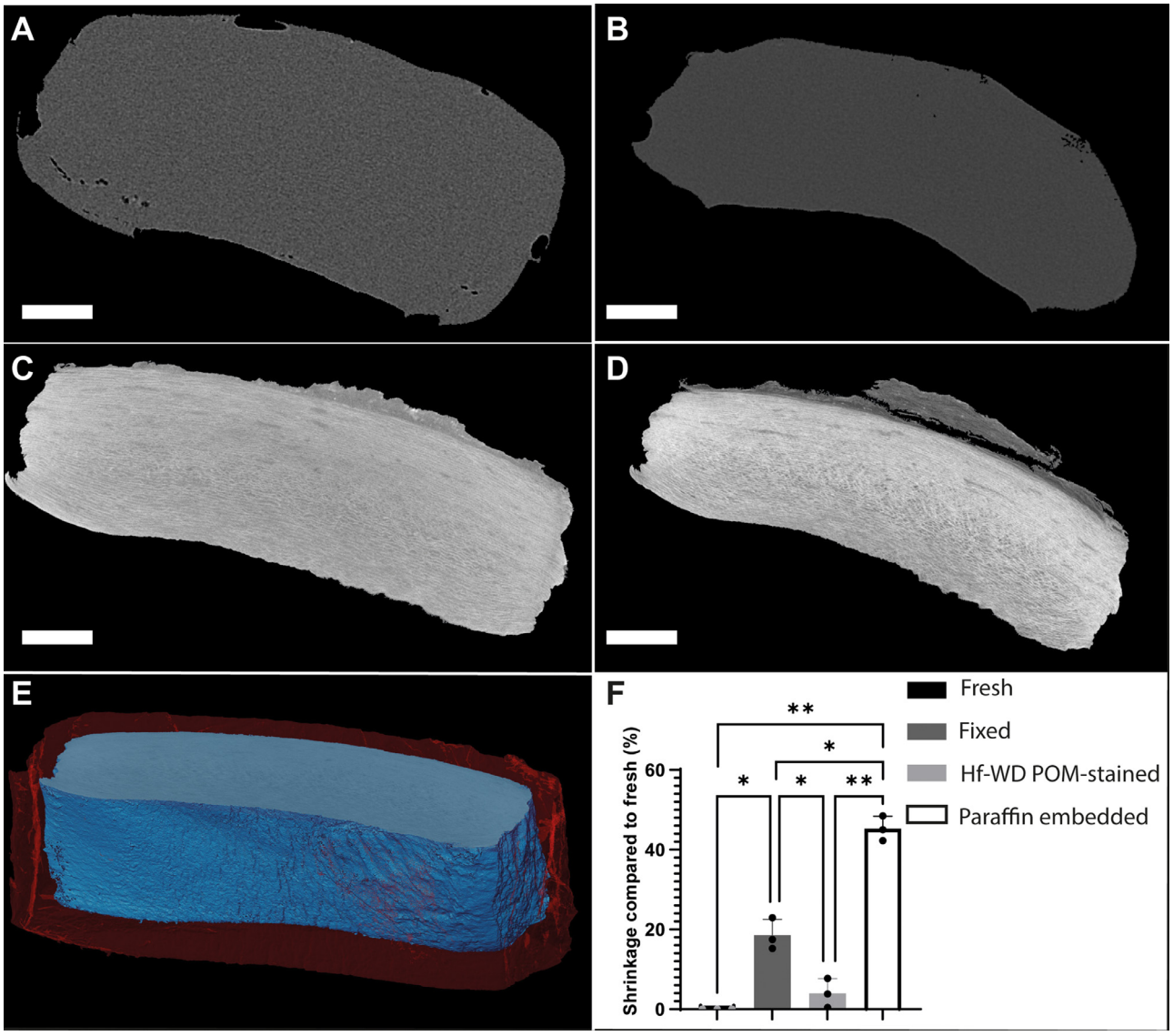


Fig. 2. Volume comparison of a piece of porcine aorta: fresh, fixed in FA, after Hf-WD POM staining, and after paraffin embedding. CECT-based sections of porcine aorta (A) fresh, (B) after fixation in FA, (C) after staining with Hf-WD POM and (D) after embedding in paraffin. (E) Overlay of CECT-based volumes after Hf-WD POM staining (red translucent) and after embedding in paraffin (blue). (F) Volume comparison between fresh, fixed, after Hf-WD POM staining, and paraffin embedding. Scalebars = 500 µm, $n = 3$, * $p \leq 0.05$, ** $p \leq 0.01$, *ns* $p > 0.05$. (For interpretation of the references to color in this figure legend, the reader is referred to the web version of this article.)

3.4. Microstructural differences between the porcine aorta, femoral artery, and vena cava

Differences in the microstructure of the different types of blood vessels in the porcine animal model were found: aorta (elastic artery), femoral artery (muscular artery), and vena cava (vein). This shows that treatment options may need to be adapted according to the blood vessel type for optimized treatment. For this reason, it is important to understand the 3D arrangement of the blood vessel wall constituents as can be obtained from CECT-based high-resolution images (Fig. 4). The relative thickness of each layer (media and adventitia) varies according to the function of the blood vessel and hence the blood vessel type (Suppl. Video 1). The aorta has the thickest medial layer relative to its full thickness with elastic lamellae throughout because it needs to be able to stretch during ventricular contraction and subsequently return to its original shape (Fig. 4A). The femoral artery has a thinner medial layer. As it is a muscular artery and is responsible for distributing the blood to the lower limbs, it is less subjected to the heart contractions and high-pressure changes and needs fewer elastic lamellae throughout its media. It has a prominent internal elastic lamina (IEL) and EEL (Fig. 4B). The vena cava is characterized by its thin medial layer compared to its thick adventitia. It is the largest vein in the body and is responsible for bringing the deoxygenated blood back to the heart and is not subjected to high blood pressures (Fig. 4C).

3.5. Quantification of structural parameters of different tissue constituents in different types of blood vessels

To better understand the 3D blood vessel wall microstructure, it is important to be able to quantify the structural parameters of its constituents. This information can be used as input for the design of optimized treatments, such as vascular grafts. In the rat and porcine aorta, the elastic lamellae in the media can be segmented to visualize their 3D arrangement and quantify their struc-

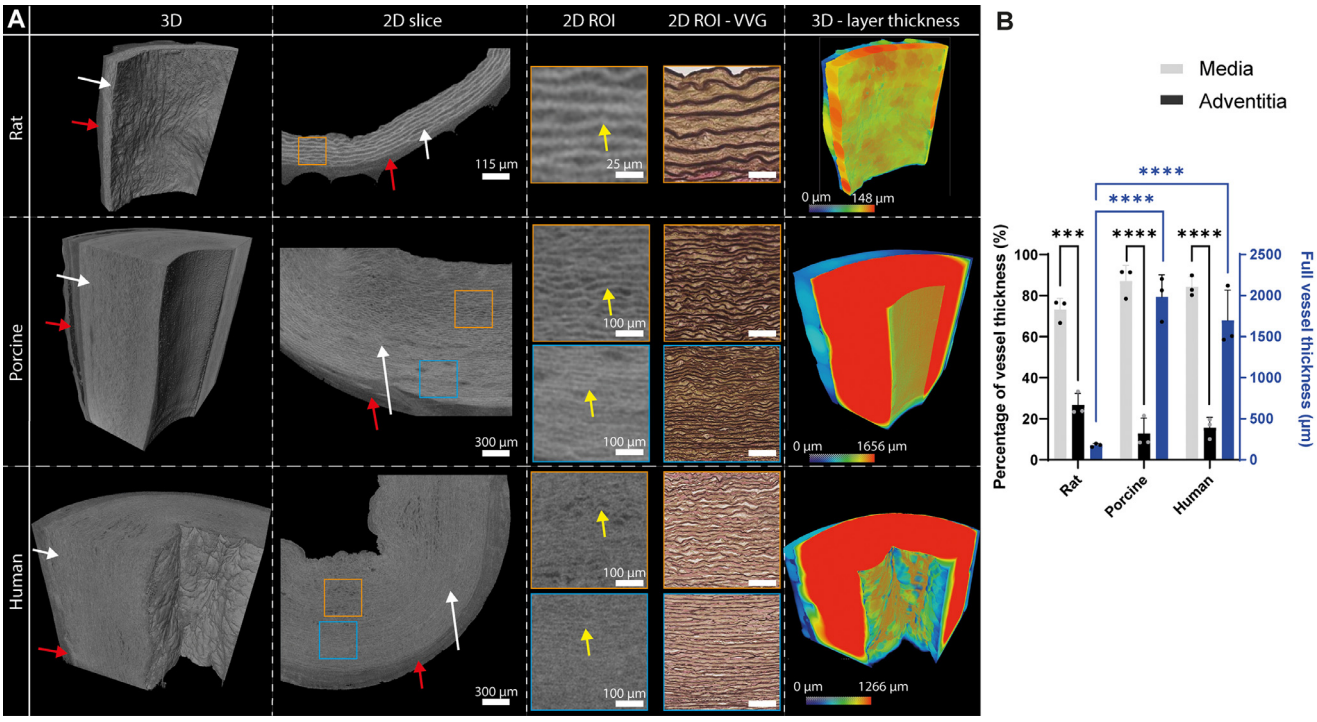


Fig. 3. Differences in microstructure between the rat, porcine and human aorta. (A) Comparison of CECT-based high-resolution images of the rat, porcine, and human aorta stained with Hf-WD POM, showing a 3D representation in the first column, a 2D slice in the second column, a comparison with classical 2D histology with Verhoeff's stain (VVG) on a small ROI in the third column and the results of the layer thickness measurements in the last column, the color-legend scalebar represents the thickness for each vessel layer. (B) Comparison between the normalized media and adventitia thickness for the three species (left Y-axis) and comparison of the full vessel thickness between the three species (right Y-axis). White arrow = media, red arrow = adventitia; yellow arrow = elastic lamella, $n = 3$, *** $p \leq 0.001$, **** $p \leq 0.0001$, *ns* $p > 0.05$. (For interpretation of the references to color in this figure legend, the reader is referred to the web version of this article.)

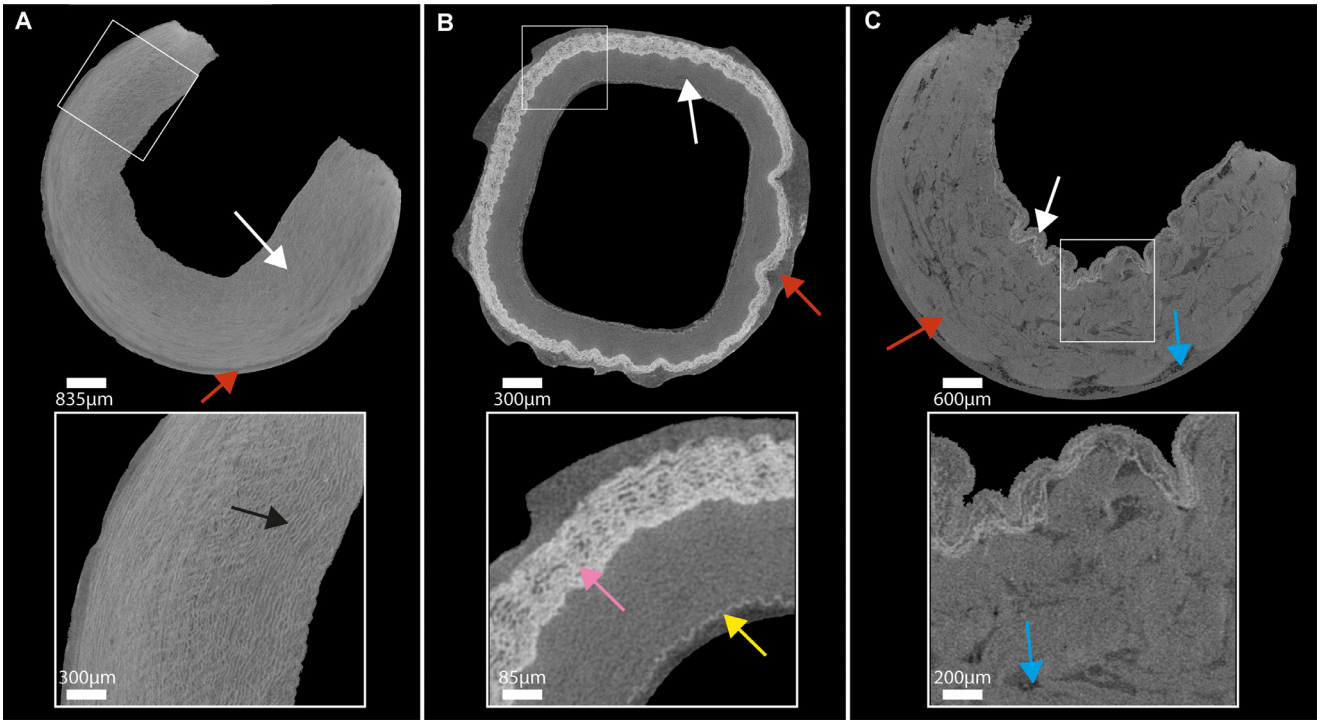


Fig. 4. Microstructural differences between the porcine aorta, femoral artery, and vena cava. CECT-based representations of the porcine (A) aorta, (B) femoral artery, and (C) vena cava. Red arrow = adventitia, white arrow = media, yellow arrow = internal elastic lamina, pink arrow = external elastic lamina, black arrow = elastic lamella, blue arrow = adipocytes. (For interpretation of the references to color in this figure legend, the reader is referred to the web version of this article.)

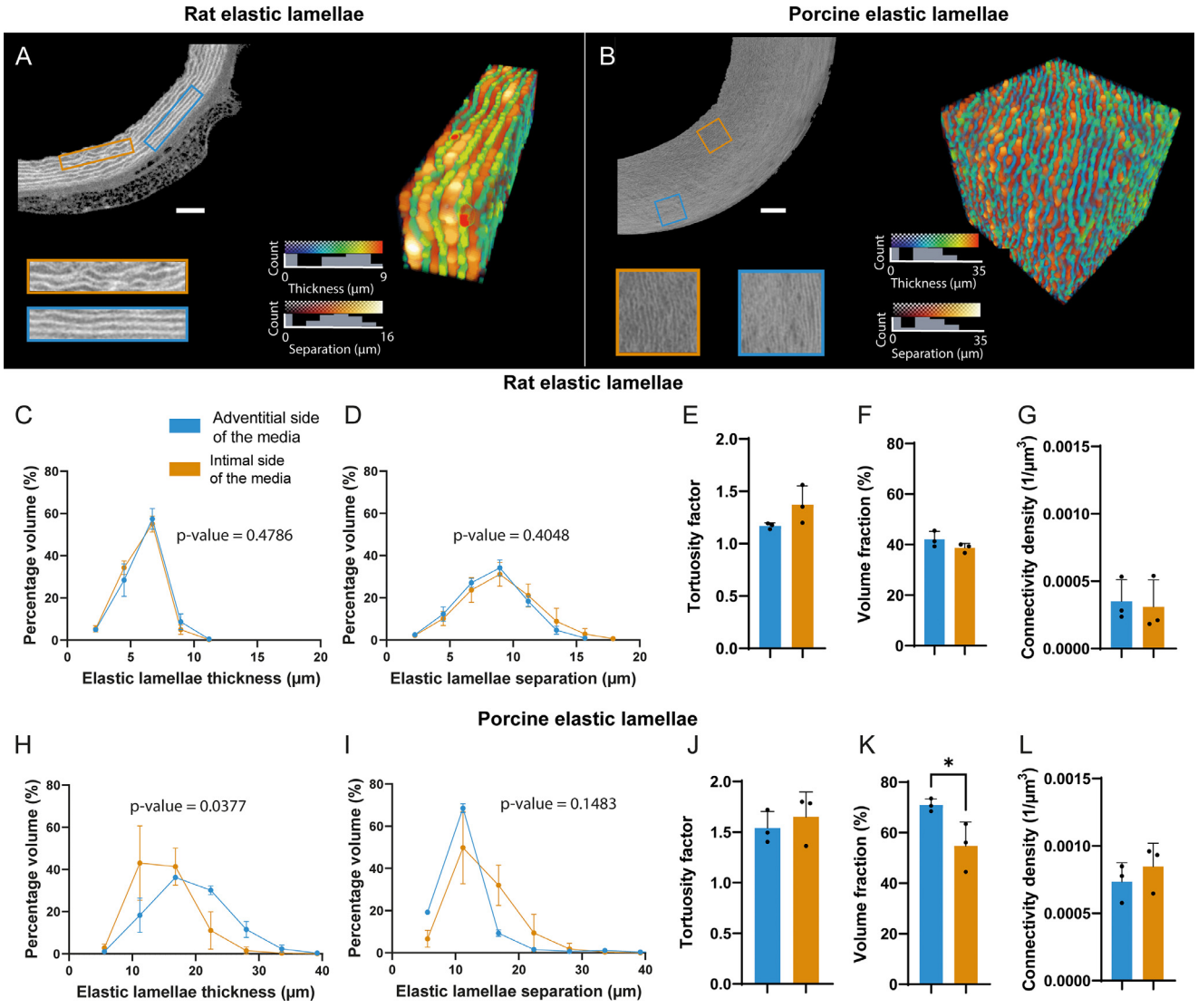
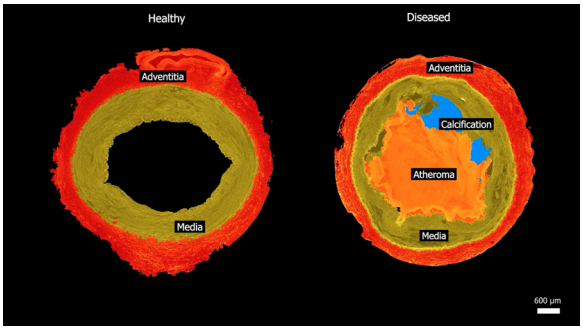


Fig. 5. Quantitative structural parameters extracted from the media of the porcine aorta. Visual differences between an ROI selected in the media, close to the intima (orange) and close to the adventitia (blue) and representative VOI with thickness and separation (distance between elastic lamellae) of the elastic lamellae represented with a color scale bar for the (A) rat aorta and (B) porcine aorta. Quantitative parameters of the elastic lamellae computed on VOIs close to the intima (orange) or close to the adventitia (blue) (each datapoint represents the average of three selected VOIs): (C,H) thickness distribution, (D,I) separation distribution, (E,J) tortuosity factor, (F,K) volume fraction, and (G,L) connectivity density. Scalebar = 100 μm for (A) and 400 μm for (B), $n = 3$, * $p \leq 0.05$, *ns* $p > 0.05$, *p-values given for graphs C, D, H, and I are for the comparison between mean values of the distributions.*(For interpretation of the references to color in this figure legend, the reader is referred to the web version of this article.)

tural parameters (Fig. 5). VOIs at the intimal and at the adventitial side of the media were selected (Fig. 5A,B) to show the differences in thickness distribution (Fig. 5C,H), average separation (Fig. 5D,I), tortuosity (Fig. 5E,J), volume fraction (Fig. 5F,K), and connectivity density (Fig. 5G,L) of the elastic lamellae depending on their location in the media. In the rat aorta, the elastic lamellae are homogeneous throughout the media. No significant differences are observed between the adventitial and intimal sides of the media for any on the structural parameters characterizing the elastic lamellae. In the porcine aorta, on the intimal side of the media, the elastic lamellae are thinner (difference in average thickness is significant with $p = 0.0377$ *) with a larger, although not significant, distance between them. The spread of the thickness distribution of the elastic lamellae is similar at the adventitial and intimal sides, indicating that the variation in thickness is the same throughout the media. It is important to note that the thicker sheets at the adventitial side can be partly explained by the fact that they are so close together (in some cases touching each other) that multiple sheets are sometimes detected as one. The larger spread of the separation distribution at the intimal side than at the adventitial side is explained by the higher variation in distance between elastic lamellae, and hence the higher tortuosity of the sheets. Additionally, their volume fraction is lower on the intimal than on the adventitial side of the media. The latter is not significant, but the variation on the tortuosity factor is much higher on the adventitial side. The connectivity density of the elastic lamellae is larger on the intimal side than on the adventitial side of the media, although not significantly. The elastic lamellae in the porcine aorta are approximately 3 times thicker than in the rat aorta. The elastic lamellae of the rat aorta are on average more wavy (higher tortuosity factor) and hence, their volume fraction is lower. It can also be observed that the average connectivity density of the elastic lamellae is lower in the rat aorta. This structural information is important because the elastic lamellae are a key constituent for assessing the mechanical behavior of the aorta.

3.6. CECT-based imaging allows to visualize and segment the different tissue constituents of an atherosclerotic human femoral artery

Using CECT, it is also possible to visualize and segment the tissue constituents of diseased blood vessels, such as atherosclerotic arteries (Video 1). A visual comparison was made between a healthy and an atherosclerotic human femoral artery. In both vessels, the media and the adventitia were segmented. In the diseased vessel, the atheroma and the calcified regions of the vessel were located and segmented.



Video 1. Segmentation of a healthy and diseased human femoral artery. CECT-based 3D representations of a (left) healthy and (right) an end-stage atherosclerotic human femoral artery. Segmentation of the different vessel layers (media and adventitia) in both vessels and segmentation of the atheroma and calcified regions in the diseased blood vessel.

3.7. The microstructure of different synthetic vascular grafts is highly variable and different compared to the native tissue

When the function of a blood vessel is compromised by disease and needs to be replaced, arterial bypass surgery can be performed. Currently used synthetic vascular grafts still lack in biocompatibility and appropriate compliance. We compared the microstructure of several currently used synthetic grafts (Fig. 6). Dacron and Gore-Tex are both composed of a single layer with homogeneous properties (Fig. 6A). The microstructure of Dacron and Gore-Tex described here does not match that of the native tissue, which is usually composed of three layers having a heterogeneous composition. Vectra does contain three self-bonded microporous layers: an inner layer (foam), a self-sealing middle layer or sheet, and an outer layer (foam), containing a coiled wire (Fig. 6A). These layers still have a homogeneous microstructure, not resembling that of the native tissue. The 3D visualization of the microstructure of the grafts with CECT is useful to compare them with native tissue and shows that their microstructure is very different. Some important structural parameters of these vascular grafts were determined: fiber thickness (Fig. 6B), separation (Fig. 6C) and volume fraction (Fig. 6D). Dacron has the thickest fibers with an average volume fraction of around 72.46 %. Gore-Tex has the smallest pores with an average volume fraction of around 77.77 %. Vectra only has an average volume fraction of 25.02 %. These parameters are interesting to compare synthetic grafts between them but it remains difficult to compare them to native tissue. In native tissue, collagen fibers and elastic sheets are present for example, and it is not always trivial or relevant to compare the fibers of the grafts to these constituents.

4. Discussion

Cardiovascular occlusive diseases are commonly treated with the help of synthetic vascular grafts [64–66]. However, the latter still fail in many cases because their functional properties are not optimized to match with those of the native tissue. The mismatch in compliance and caliber, and the stress concentration at the interface between graft and native tissue lead to abnormal shear stresses at the vessel wall, still creating a gap in functional behavior between both [24]. Since 'form follows function' and vice versa [67], the microstructure of the current synthetic vascular grafts might not be appropriate to match their functional properties with those of the native tissue. Native vessels are composed of different functional layers, which themselves also have an inhomogeneous structure. As an example, in the porcine model, the medial layer, one of the three main layers of the aorta, contains elastic lamellae with varying waviness and thickness from one side to the other, as shown in our study (Fig. 5). Additionally, often the same synthetic grafts with only a difference in diameter are used for the different types of blood vessels, which have a different microstructure. All this makes the microstructural comparison and matching of the functional properties of synthetic vascular grafts with native tissue challenging. We were able, in this study, to determine the microstructural properties, such as the fiber thickness, the fiber separation and the fiber volume fraction of the most common clinically used synthetic grafts. Dacron and Gore-Tex are currently clinically used as vascular conduits, but they both have a homogeneous microstructure throughout, explaining some of the many issues that remain in terms of biocompatibility. Vectra is currently not used as a bypass graft for diseased vessels, but rather as an arteriovenous graft to optimize hemodialysis, by increasing pressure and blood flow through the vein. Its microstructure is not yet optimal but its layered structure provides insights for the design of new materials that more accurately replicate the functional behavior of the artery. Although the comparison between grafts and native tissue, based on structural parameters, is challenging, the 3D microCT-based images of the grafts and the 3D CECT-based images of the native tissue are helpful to further optimize the design of grafts. New innovative methodologies involving vascular tissue engineering have been explored to mitigate the poor patency rates of synthetic grafts, especially for small-caliber grafts. They involve the vascular cell seeding of polymeric scaffolds [68–70]. However, efforts are still required to obtain ideal mechanical and biological performance. To improve treatment options, microstructural knowledge on current synthetic grafts as well as of native tissue is crucial.

In the literature, experimental evaluation of pathologies and their treatments is mostly done on one selected blood vessel type in one animal. Only few studies report microstructural differences between blood vessels in different species or differences between types of blood vessels [27,28]. As porcine animal models are often used to study human heart valve-related diseases, under the assumption that these tissues are similar, some groups have investigated porcine and/or human aortic tissues, focusing on the ascending aorta and heart valves [27,71]. According to their results, care should be taken when using porcine animal models to study human diseases. However, their microstructural analysis is based on classical 2D histological techniques only. In the current study, we investigated microstructural differences between three species (rat, porcine, human) and between three porcine blood vessel types (aorta, femoral artery, vena cava). The tunica media and tunica adventitia were segmented for all blood vessels. The tunica intima is composed of a single layer of endothelial cells and could not be readily visualized at the spatial resolutions we imaged. Visual differences between the rat, porcine, and human aortas and femoral arteries were found mainly in terms of spatial arrangement, shape of the elastic lamellae and microstructural arrangement of the external elastic lamina. The ratio in thickness between the media and adventitia is similar for all species in the aorta (elastic artery) with a thicker media compared to the adventitia,

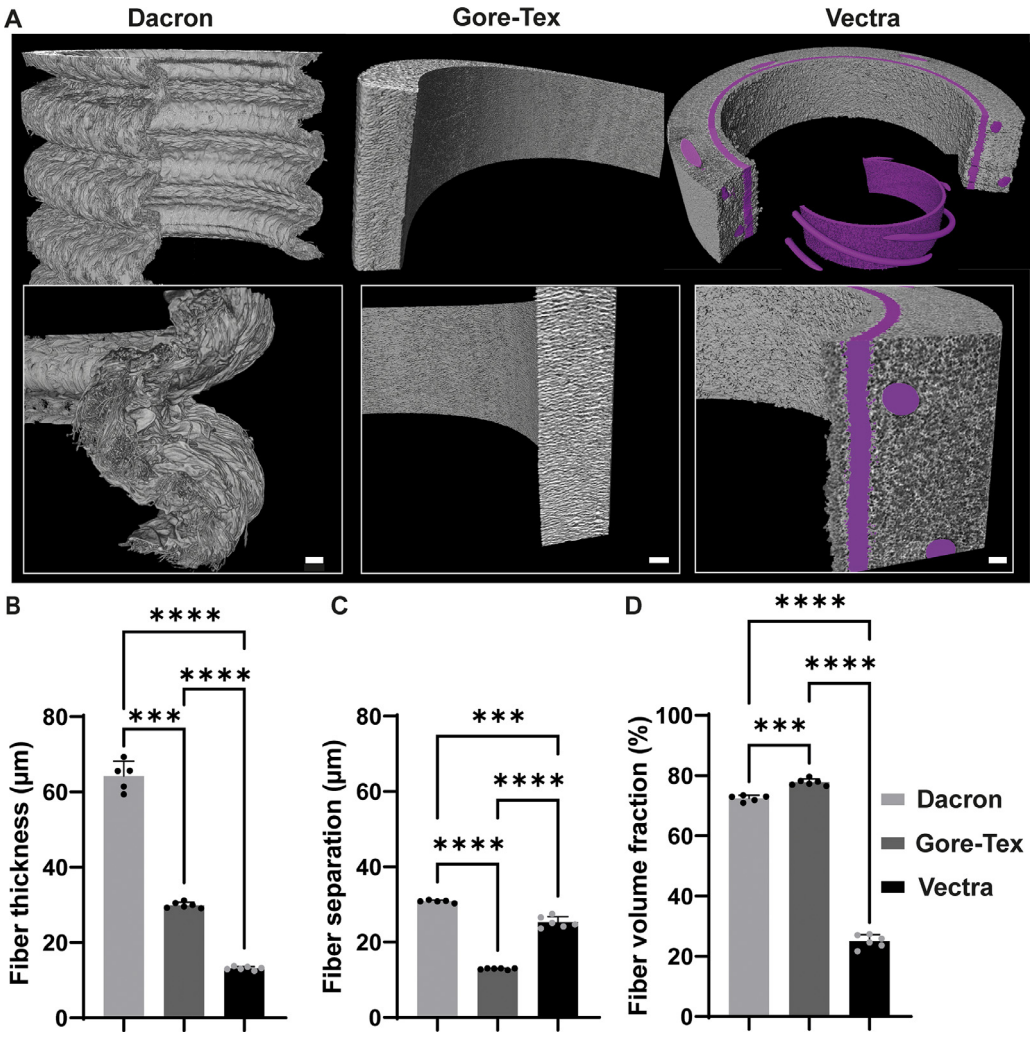


Fig. 6. Microstructural analysis of synthetic vascular grafts commercially available. CECT-based 3D representations of (A) Dacron, Gore-Tex, and Vectra and comparison of fiber (B) thickness, (C) separation, and (D) volume faction. Scalebars = 200 µm, $n = 5$ (Dacron), $n = 6$ (Gore-Tex and Vectra), *** $p \leq 0.001$, **** $p \leq 0.0001$.

containing much more elastic tissue than the media of the femoral artery (muscular artery) to allow it to maintain a relatively constant pressure gradient despite the pumping action of the heart [31]. In the femoral artery, the thickness ratio between media and adventitia is highly variable among species but the media contains much more SMCs and less elastic tissue. In terms of full vessel thickness, the rat aorta is significantly thinner than the porcine and human aorta and the rat femoral artery is significantly thinner than the porcine and human femoral artery. Between the aorta, femoral artery, and vena cava, differences mainly were detected concerning the relative thickness of the different layers and their content in elastic lamellae versus collagen and SMCs. Additionally, when computing different structural parameters of the elastic lamellae in the media of the rat and porcine aortas, it was shown that the variation throughout the media is very different for both species. In the rat aorta, the elastic lamellae are much more homogeneous throughout the medial layer than for the porcine aorta. In the current literature, parameters such as breaks in the elastic lamellae are often counted manually on classical 2D histological slices [72–74] or shown visually in scanning electron microscopy images [75]. In phase-contrast or synchrotron microCT, some parameters have been quantified such as, waviness [76], and volume fraction [41]. However, to detect breaks in the elastin, manual annotations are often still required [40]. The advantage of CECT is that after segmentation of the elastic lamellae, structural parameters can be computed automatically and in 3D. However, it remains non-trivial to quantify change in the structure of the elastic lamellae.

In this study, we have mainly imaged small tissue sections to obtain high resolution images. However, it is also possible to image the entire circumference of the different blood vessels. This is sometimes at the cost of a loss in resolution, however, this is necessary to study pathological specimens, such as aneurysms or atherosclerotic plaque, as shown in Video 1. Indeed, for CECT imaging to be widely used, it is important to show that it is possible to apply the technique to diseased heterogeneous blood vessels. We showed the possibility to image and segment an end-stage atherosclerotic human femoral artery. After segmentation, it is possible to obtain quantitative information such as volume of calcified tissue and volume of the atheroma. It also allows to study where onsets of calcifications are occurring and how the microstructural constituents, such as the internal and external elastic lamina are affected by the disease. This is important for better understanding the pathogenesis of atherosclerosis, which is still not fully understood [77].

A limitation of our study is that we focused on the imaging of elastin as constituent because we did not achieve sufficient resolution to image the collagen fibers. However, collagen fibers and

their orientation have an important impact on the mechanical behavior and are thus an important wall constituent. Moreover, due to time constraints and limited sample availability, only three biological samples per group were assessed. More samples should be imaged in the future. The goal was to show a proof of concept for the quantitative assessment of blood vessel wall structural properties using CECT-based imaging.

To validate CECT data, often classical 2D histology is used [40,47,78]. For visual and qualitative validation, this might be appropriate. However, in this study, we found evidence that classical 2D histology cannot be used to validate the thickness measurements of the different wall layers nor for the structural analysis of the tissue constituents. Our analysis showed a shrinkage of the tissue due to fixation in 4% FA of around 18.5%. This shrinkage can be explained due to the cross-linking of the proteins in the tissue [79–82]. The staining with Hf-WD POM caused consistent swelling of the tissues of around 17.9%. Swelling was also observed upon staining with Mono-WD POM (data not shown). We hypothesize that this is caused by osmotic effects [83]. This means that when POMs and other ions enter the tissue, this seems to be accompanied by an osmotically-driven flow of water molecules in the tissue, leading to swelling. When we then prepare the tissue for sectioning for classical 2D histology (embedding in paraffin), a more significant decrease in volume of around 43% compared to the Hf-WD POM-stained tissue was found. We have also seen that the sectioning and colorimetric staining after paraffin embedding can cause additional damage/changes to the microstructure of the tissue (disruption of the adventitial layer of the wall in the aorta and femoral artery, data not shown). Both the substantial tissue shrinkage as well as the potential tissue disintegration with classical 2D histology show the benefit of using CECT for conservation of the tissue integrity for quantitative microstructural characterization, provided that the appropriate CESA is used that does not cause any tissue deformation.

We evaluated in this study the use of two polyoxometalates (POMs), Mono-WD POM and Hf-WD POM, for CECT imaging of the vascular tissues. Hf-WD POM and Mono-WD POM are both negatively charged while tropoelastin, elastin's subunit, is likely to be positively charged at physiological pH. On the contrary, the other proteins present in the blood vessel wall (mainly collagen and fibrillin) are likely to have a negative net charge at physiological pH (net charge at pH=7.4 determined with Expasy [85] and ClustalW). The POMs are thus more likely to interact with elastin compared to the other proteins. Concerning their diffusion kinetics, we found that, even though staining time and therefore sample preparation time is reduced using Mono-WD POM, Hf-WD POM allowed a better visualization of the microstructure of the blood vessel wall, allowing the distinction of the individual elastic lamellae mostly present in the medial layer of the aorta. It must be noted that the Mono-WD POM and Hf-WD POM concentrations used in this study lead to a molar concentration of Mono-WD POM that is approximately twice has high as that of Hf-WD POM. This should be considered when comparing staining times. However, we assume that at the same molar concentration, the Mono-WD POM will still penetrate the tissue faster compared to the Hf-WD POM given that it reaches the plateau four times faster on average. Independently of the staining time, the specificity, and hence the binding mechanisms of Hf-WD POM are different from those of Mono-WD POM. The slow diffusion of the Hf-WD POM most likely comes from a stronger POM-protein interaction for this compound [84]. Hf-WD POM has one Lewis acidic Hafnium atom that has oxidation state +IV, which should improve interaction with proteins, such as elastin [84]. This is not the case for Mono-WD POM. Ongoing research in our group is currently focusing on better understanding the link between the interactions and the diffusion of the CESAs.

5. Conclusion

Cardiovascular diseases are still a major cause of death and to enhance our treatment strategies, improved knowledge on the native tissue microstructure of the blood vessels could be useful. Indeed, we emphasized the gap that still remains between existing vascular replacement grafts and the native vascular tissue. We have shown that Hf-WD POM-based CECT combined with advanced image processing and analysis provides a way to visualize the 3D microstructure and quantify the structural parameters of the native blood vessel wall and synthetic grafts. We showed that this technique is advantageous compared to classical 2D histology for structural analysis, which induces tissue deformation during sample preparation and can thus not be used to extract quantitative data. Moreover, CECT allows to avoid paraffinization and tissue degradation and provides 3D information instead of only 2D. We indicated the differences that exist in the microstructure of the blood vessels of different species to highlight the importance of carefully choosing an animal model when studying a disease or disease treatment. In the porcine model, the differences between blood vessels were also highlighted to show that disease treatments should also consider blood vessel type. From the CECT-based representations of the blood vessels, we extracted quantitative information, such as thickness, separation, volume fraction, and tortuosity of the elastin sheets of the aorta. This information leads to a better understanding of the native blood vessel wall. It is important knowledge to further improve the current disease treatments, such as providing input for new and optimized design of synthetic vascular grafts.

Declaration of Competing Interest

The authors declare that they have no known competing financial interests or personal relationships that could have appeared to influence the work reported in this paper.

Acknowledgments

We would like to thank Sandrine Horman and Marie Octave (UCLouvain) for providing the rat aortas and femoral arteries, Ramadan Jashari (European Homograft Bank) for providing the human femoral arteries, Laurent De Kerchove de Denterghem (Cliniques universitaires Saint-Luc, UCLouvain) for supplying the human aortas, Lukas Van Hoof (KU Leuven) for the porcine femoral arteries, and Inge Fourneau and Sabrina Houthoofd for providing the atherosclerotic human fermoal artery (UZ Leuven - KU Leuven). We would also like to thank Pierre Schneidewind (UCLouvain) for the help with the 2D histological sectioning and staining.

Funding

L.L. is funded by the UClouvain, Belgium (assistant position) and an FSR project – Projets Fonds de Recherche Spécial Jeunes Académiques – Fédération Wallonie-Bruxelles. T.B. acknowledges the French Community of Belgium in the framework of a FRIA grant (40004158). T.B. and M.P. acknowledge the support from an FWO project (FWO; grant G088218N). W.E.A. and G.K. acknowledge the Action de Recherche Concertée (ARC 19/24-097) - Fédération Wallonie-Bruxelles. G.P. acknowledges the support from the SBO project of the Research Foundation Flanders (FWO; grant S007219N). The CECT data was generated at the KU Leuven XCT core facility and financed by the Hercules Foundation (project AKUL 13/47). Avizo 2022.1 (ThermoFisher Scientific, France) software acquisition was supported by the Fonds de la Recherche Scientifique – (FNRS - EQP - Tomo4D-U.N069.20)

Supplementary materials

Supplementary material associated with this article can be found, in the online version, at doi:10.1016/j.actbio.2023.04.013.

References

[1] A.A. Postnov, P.C. D'Haese, E. Neven, N.M. De Clerck, V.P. Persy, Possibilities and limits of X-ray microtomography for in vivo and ex vivo detection of vascular calcifications, Int. J. Cardiovasc. Imaging 25 (2009) 615–624, doi:10.1007/s10554-009-9459-9.

[2] Y. Momiyama, R. Ohmori, Z.A. Fayad, N. Tanaka, R. Kato, H. Taniguchi, M. Nagata, F. Ohsuzu, The LDL-cholesterol to HDL-cholesterol ratio and the severity of coronary and aortic atherosclerosis, Atherosclerosis 222 (2012) 577–580, doi:10.1016/j.atherosclerosis.2012.03.023.

[3] G. Jondeau, C. Boileau, Genetics of thoracic aortic aneurysms, Curr. Atheroscler. Rep. 14 (2012) 219–226, doi:10.1007/s11883-012-0241-4.

[4] M. Takigawa, T. Yoshimuta, K. Akutsu, S. Takeshita, N. Yokoyama, Prevalence and predictors of coexistent silent atherosclerotic cardiovascular disease in patients with abdominal aortic aneurysm without previous symptomatic cardiovascular diseases, Angiology 63 (2012) 380–385, doi:10.1177/0003319711419359.

[5] A. Sekikawa, C. Shin, J.D. Curb, E. Barinas-Mitchell, K. Masaki, A. El-Saed, T.B. Seto, R.H. Mackey, J. Choo, A. Fujiyoshi, K. Miura, D. Edmundowicz, L.H. Kuller, H. Ueshima, K. Sutton-Tyrrell, Aortic stiffness and calcification in men in a population-based international study, Atherosclerosis 222 (2012) 473–477, doi:10.1016/j.atherosclerosis.2012.03.027.

[6] A. Tsamis, A. Rachev, N. Stergiopulos, A constituent-based model of age-related changes in conduit arteries, Am. J. Physiol. - Hear. Circ. Physiol. 301 (2011) 1286–1301, doi:10.1152/ajpheart.00570.2010.

[7] Y. Orcel, É. Camilleri, A. Dehaene, Dissection aortique, Rev. Prat. 68 (2018) 752, doi:10.1016/b978-2-294-76093-8.00007-x.

[8] A. Matsushita, S. Manabe, M. Tabata, T. Fukui, T. Shimokawa, S. Takanashi, Efficacy and pitfalls of transapical cannulation for the repair of acute type A aortic dissection, Ann. Thorac. Surg. 93 (2012) 1905–1909, doi:10.1016/j.athoracsur.2012.02.036.

[9] S. Lu, X. Sun, T. Hong, S. Yang, K. Song, H. Lai, K. Hu, C. Wang, Bilateral versus unilateral antegrade cerebral perfusion in arch reconstruction for aortic dissection, Ann. Thorac. Surg. 93 (2012) 1917–1920, doi:10.1016/j.athoracsur.2012.02.090.

[10] A.H. Davies, The seriousness of chronic venous disease: a review of real-world evidence, Adv. Ther. 36 (2019) 5–12, doi:10.1007/s12325-019-0881-7.

[11] Y.J. Youn, J. Lee, Chronic venous insufficiency and varicose veins of the lower extremities, Korean J. Intern. Med. 34 (2019) 269–283, doi:10.3904/kjim.2018.230.

[12] A. Mansilha, J. Sousa, Pathophysiological mechanisms of chronic venous disease and implications for venoactive drug therapy, Int. J. Mol. Sci. 19 (2018) 1–21, doi:10.3390/ijms19061669.

[13] R.A. Jonas, F.J. Schoen, R.J. Levy, A.R. Castaneda, Biological sealants and knitted Dacron: porosity and histological comparisons of vascular graft materials with and without collagen and fibrin glue pretreatments, Ann. Thorac. Surg. 41 (1986) 657–663, doi:10.1016/S0003-4975(10)63083-4.

[14] R.A. Jonas, G. Ziemer, F.J. Schoen, L. Britton, A.R. Castaneda, A new sealant for knitted Dacron prostheses: minimally cross-linked gelatin, J. Vasc. Surg. 7 (1988) 414–419, doi:10.1016/0741-5214(88)90437-5.

[15] C.A. Bustos, C.M. García-Herrera, D.J. Celentano, Mechanical characterisation of Dacron graft: experiments and numerical simulation, J. Biomech. 49 (2016) 13–18, doi:10.1016/j.jbiomech.2015.11.014.

[16] M. Amabili, P. Balasubramanian, I. Breslavsky, G. Ferrari, E. Tubaldi, Viscoelastic characterization of woven Dacron for aortic grafts by using direction-dependent quasi-linear viscoelasticity, Journal of the mechanical behavior of biomedical materials 82 (2018) 282–290, doi:10.1016/j.jmbbm.2018.03.038.

[17] G. Penford, D. Quandt, C. Mehta, V. Bhole, R. Dhillon, A. Seale, O. Stumper, Stenting and overdilating small Gore-Tex vascular grafts in complex congenital heart disease, Catheter. Cardiovasc. Interv. 91 (2018) 71–80, doi:10.1002/ccd.27310.

[18] J. Chlupác, E. Filová, L. Bačáková, Blood vessel replacement: 50 years of development and tissue engineering paradigms in vascular surgery, Physiol. Res. 58 (2009) 119–140, doi:10.33549/physiolres.931918.

[19] L. Xue, H.P. Greisler, Biomaterials in the development and future of vascular grafts, J. Vasc. Surg. 37 (2003) 472–480, doi:10.1067/mva.2003.88.

[20] C. Spadaccio, A. Rainer, R. Barbato, M. Trombetta, M. Chello, B. Meyns, The long-term follow-up of large-diameter Dacron® vascular grafts in surgical practice: a review, J. Cardiovasc. Surg. (Torino). 60 (2019) 501–513, doi:10.23736/S0021-9509.16.08061-7.

[21] M. Amabili, P. Balasubramanian, G. Ferrari, G. Franchini, F. Giovanniello, E. Tubaldi, Identification of viscoelastic properties of Dacron aortic grafts subjected to physiological pulsatile flow, J. Mech. Behav. Biomed. Mater. 110 (2020) 103804, doi:10.1016/j.jmbbm.2020.103804.

[22] F.W. LoGerfo, W.C. Quist, M.D. Nowak, H.M. Crawshaw, C.C. Haudenschild, Downstream anastomotic hyperplasia. A mechanism of failure in Dacron® arterial grafts, Ann. Surg. 197 (1983) 479–483, doi:10.1097/00000658-198304000-00018.

[23] C.H. Chew, B.L. Sheu, A. Chen, W.T. Huang, T.M. Cheng, C.M. Shih, A. Chang, C.C. Chen, Tissue-engineered vascular graft with co-culture of smooth muscle cells and human endothelial vein cells on an electrospun poly(Lactic-co-glycolic acid) microtube array membrane, Membranes (Basel) 11 (2021), doi:10.3390/membranes11100732.

[24] S. Sarkar, H.J. Salacinski, G. Hamilton, A.M. Seifalian, The mechanical properties of infrainguinal vascular bypass grafts: their role in influencing patency, Eur. J. Vasc. Endovasc. Surg. 31 (2006) 627–636, doi:10.1016/j.ejvs.2006.01.006.

[25] A. Tiwari, K.S. Cheng, H. Salacinski, G. Hamilton, A.M. Seifalian, Improving the patency of vascular bypass grafts: The role of suture materials and surgical techniques on reducing anastomotic compliance mismatch, Eur. J. Vasc. Endovasc. Surg. 25 (2003) 287–295, doi:10.1053/ejvs.2002.1810.

[26] P.D. Ballyk, C. Walsh, J. Butany, Compliance mismatch may promote graft–artery intimal hyperplasia by altering suture-line stresses, J. Biomech. 31 (1997) 229–237, doi:10.1016/S0197-3975(97)00111-5.

[27] C. Martin, T. Pham, W. Sun, Significant differences in the material properties between aged human and porcine aortic tissues, Eur. J. Cardio-Thoracic Surg. 40 (2011) 28–34, doi:10.1016/j.ejcts.2010.08.056.

[28] J.M. Mattson, Y. Zhang, Structural and functional differences between porcine aorta and vena cava, ASME, J Biomech Eng 139 (7) (2017) 071007, doi:10.1115/1.4036261.

[29] S.S. Shahid, R.D. Johnston, C. Smekens, C. Kerskens, R. Gaul, B. Tornifoglio, A.J. Stone, C. Lally, Exploring arterial tissue microstructural organization using non-Gaussian diffusion magnetic resonance schemes, Sci. Rep. 11 (2021) 1–13, doi:10.1038/s41598-021-01476-z.

[30] D. Weiss, C. Cavinato, A. Gray, A. Ramachandra, J. Humphrey, M. Latorre, D. Weiss, C. Cavinato, A. Gray, A. Ramachandra, S. Avril, D. Weiss, C. Cavinato, A. Gray, A.B. Ramachandra, S. Avril, J.D. Humphrey, M. Latorre, Mechanics-driven mechanobiological mechanisms of arterial tortuosity, Sci. Adv. 6.49 (2020) eabd3574, doi:10.1126/sciadv.abd3574.

[31] William D. Tucker, Yingyot Arora, Kunal Mahajan, Anatomy, Blood Vessels, StatPearls Publishing, Treasure Island (Florida, USA), 2021 https://www.ncbi.nlm.nih.gov/books/NBK470401/.

[32] O.P. Choudhary, P. Ka, Scanning electron microscope: advantages and disadvantages in imaging components, Int. J. Curr. Microbiol. Appl. Sci. 6 (2017) 1877–1882, doi:10.20546/ijcmas.2017.605.207.

[33] P.N. Lewis, R.D. Young, R.B. Souza, A.J. Quantock, K.M. Meek, Contrast-enhanced tissue processing of fibrillin-rich elastic fibres for 3D visualization by volume scanning electron microscopy, Methods Protoc. 4 (2021), doi:10.3390/mps4030056.

[34] P.O. Bayguinov, D.M. Oakley, C.C. Shih, D.J. Geanon, M.S. Joens, J.A.J. Fitzpatrick, Modern laser scanning confocal microscopy, Curr. Protoc. Cytom. 85 (2018) 1–17, doi:10.1002/cpcy.39.

[35] M.K. O'Connell, S. Murthy, S. Phan, C. Xu, J.A. Buchanan, R. Spilker, R.L. Dalman, C.K. Zarins, W. Denk, C.A. Taylor, The three-dimensional micro- and nanostructure of the aortic medial lamellar unit measured using 3D confocal and electron microscopy imaging, Matrix Biol. 27 (2008) 171–181, doi:10.1016/j.matbio.2007.10.008.

[36] O. Fritze, M. Schleicher, K. König, K. Schenke-Layland, U. Stock, C. Harasztosi, Facilitated noninvasive visualization of collagen and elastin in blood vessels, Tissue Eng. - Part C Methods 16 (2010) 705–710, doi:10.1089/ten.tec.2009.0309.

[37] N.E. Buglak, J. Lucitti, P. Ariel, S. Maiocchi, F.J. Miller, E.S.M. Bahnson, Light sheet fluorescence microscopy as a new method for unbiased three-dimensional analysis of vascular injury, Cardiovasc. Res. 117 (2021) 520–532, doi:10.1093/cvr/cvaa037.

[38] B.T. Ledford, A.W. Akerman, K. Sun, D.C. Gillis, J.M. Weiss, J. Vang, S. Willcox, T.D. Clemons, H. Sai, R. Qiu, M.R. Karver, J.D. Griffith, N.D. Tsihlis, S.I. Stupp, J.S. Ikonomidis, M.R. Kibbe, Peptide amphiphile supramolecular nanofibers designed to target abdominal aortic aneurysms, ACS Nano 16 (2022) 7309–7322, doi:10.1021/acsnano.1c06258.

[39] A.E. Cartaya, S. Maiocchi, S. Torzone, Geri Messinger, E.S.M.B., Application of machine learning for volumetric analysis of atherosclerotic burden, BioRxiv (2022), doi:10.1101/2022.12.23.521811.

[40] G. Logghe, B. Trachet, L. Aslanidou, P. Villaneuva-Perez, J. De Backer, N. Stergiopulos, M. Stampanoni, H. Aoki, P. Segers, Propagation-based phase-contrast synchrotron imaging of aortic dissection in mice: from individual elastic lamella to 3D analysis, Sci. Rep. 8 (2018) 1–11, doi:10.1038/s41598-018-20673-x.

[41] J. López-Guimet, L. Peña-Pérez, R.S. Bradley, P. García-Canadilla, C. Disney, H. Geng, A.J. Bodey, P.J. Withers, B. Bijnens, M.J. Sherratt, G. Egea, MicroCT imaging reveals differential 3D micro-scale remodelling of the murine aorta in ageing and marfan syndrome, Theranostics 8 (2018) 6038–6052, doi:10.7150/thno.26598.

[42] A. Ben Zemzem, A. Genevaux, A. Wahart, A.J. Bodey, S. Blaise, B. Romier-Crouzet, J. Jonquet, C. Bour, R. Cogranne, P. Beauseroy, M. Dauchez, M.J. Sherratt, L. Debelle, S. Almagro, X-ray microtomography reveals a lattice-like network within aortic elastic lamellae, FASEB J. 35 (2021) 1–11, doi:10.1096/fj.202100323RR.

[43] M. Truong, T. Dreier, J. Wassélius, L. Sundius, A. Persson, G. Lovric, A. Bonnin, I. Goncalves, M. Bech, Sub-micrometer morphology of human atherosclerotic plaque revealed by synchrotron radiation-based μCT—a comparison with histology, PLoS One 17 (2022) 1–18, doi:10.1371/journal.pone.0265598.

[44] L. Leyssens, C. Pestiaux, G. Kerckhofs, A review of ex vivo x-ray microfocus computed tomography-based characterization of the cardiovascular system, Int. J. Mol. Sci. 22 (2021) 3263, doi:10.3390/ijms22063263.

[45] T.D. Butters, S.J. Castro, T. Lowe, Y. Zhang, M. Lei, P.J. Withers, H. Zhang, Optimal iodine staining of cardiac tissue for X-ray computed tomography, PLoS One 9 (2014) 1–6, doi:10.1371/journal.pone.0105552.
[46] R. Balint, T. Lowe, T. Shearer, Optimal contrast agent staining of ligaments and tendons for X-ray computed tomography, PLoS One 11 (2016), doi:10.1371/journal.pone.0153552.
[47] T.S. Self, A.M. Ginn-Hedman, C.N. Kaulfus, A.E. Newell-Fugate, B.R. Weeks, C.L. Heaps, Iodine-enhanced micro-computed tomography of atherosclerotic plaque morphology complements conventional histology, Atherosclerosis 313 (2020) 43–49, doi:10.1016/j.atherosclerosis.2020.09.012.
[48] P.J. Dunmore-Buyze, E. Tate, F.L. Xiang, S.A. Detombe, Z. Nong, J.G. Pickering, M. Drangova, Three-dimensional imaging of the mouse heart and vasculature using micro-CT and whole-body perfusion of iodine or phosphotungstic acid, Contrast Media Mol. Imaging 9 (2014) 383–390, doi:10.1002/cmmi.1588.
[49] M. Nierenberger, Y. Rémond, S. Ahzi, P. Choquet, Assessing the three-dimensional collagen network in soft tissues using contrast agents and high resolution micro-CT: application to porcine iliac veins, Comptes Rendus - Biol. 338 (2015) 425–433, doi:10.1016/j.crvi.2015.04.009.
[50] Y. Dawood, G.J. Strijkers, J. Limpens, R.J. Oostra, B.S. de Bakker, Novel imaging techniques to study postmortem human fetal anatomy: a systematic review on microfocus-CT and ultra-high-field MRI, Eur. Radiol. 30 (2020) 2280–2292, doi:10.1007/s00330-019-06543-8.
[51] P. Vickerton, J. Jarvis, N. Jeffery, Concentration-dependent specimen shrinkage in iodine-enhanced microCT, J. Anat. 223 (2013) 185–193, doi:10.1111/joa.12068.
[52] K. Degenhardt, A.C. Wright, D. Horng, A. Padmanabhan, J.A. Epstein, Rapid 3D phenotyping of cardiovascular development in mouse embryos by micro-CT with iodine staining, Circ. Cardiovasc. Imaging 3 (2010) 314–322, doi:10.1161/CIRCIMAGING.109.918482.
[53] J. Buytaert, J. Goyens, D. De Greef, P. Aerts, J. Dirckx, Volume shrinkage of bone, brain and muscle tissue in sample preparation for micro-CT and light sheet fluorescence microscopy (LSFM), Microsc. Microanal. 20 (2014) 1208–1217, doi:10.1017/S1431927614001329.
[54] S. de Bournonville, S. Vangrunderbeeck, H.G.T. Ly, C. Geeroms, W.M. De Borggraeve, T.N. Parac-Vogt, G. Kerckhofs, Exploring polyoxometalates as non-destructive staining agents for contrast-enhanced microfocus computed tomography of biological tissues, Acta Biomater. 105 (2020) 253–262, doi:10.1016/j.actbio.2020.01.038.
[55] A. Maes, C. Pestiaux, A. Marino, T. Balcaen, L. Leyssens, S. Vangrunderbeeck, G. Pyka, W.M. De Borggraeve, L. Bertrand, C. Beauloye, S. Horman, M. Wevers, G. Kerckhofs, Cryogenic contrast-enhanced MicroCT: a nondestructive approach to 3D quantitative histopathology of soft biological tissues, Under Rev. Int. Peer-Rev. J. 13 (2022) 1–14, doi:10.1038/s41467-022-34048-4.
[56] A.P. Ginsberg, Inorganic syntheses, Inorg. Synth. 1 (2007) 1–197, doi:10.1002/9780470132326.
[57] C.N. Kato, A. Shinohara, K. Hayashi, K. Nomiya, Syntheses and X-ray crystal structures of zirconium(IV) and hafnium(IV) Complexes containing monovacant wells−Dawson and keggin polyoxotungstates, Inorg. Chem. 45 (2006) 8108–8119, doi:10.1021/ic060656e.
[58] A. Misra, K. Kozma, C. Streb, M. Nyman, Beyond Charge balance: countercations in polyoxometalate chemistry, Angew. Chem. - Int. Ed. 59 (2020) 596–612, doi:10.1002/anie.201905600.
[59] J. Al Shakarchi, N. Inston, Early cannulation grafts for haemodialysis: an updated systematic review, J. Vasc. Access. 20 (2019) 123–127, doi:10.1177/1129729818776571.
[60] S.D. Rawson, J. Maksimcuka, P.J. Withers, S.H. Cartmell, X-ray computed tomography in life sciences, BMC Biol. 18 (2020) 21, doi:10.1186/s12915-020-0753-2.
[61] A. Maes, Contrast-team/histogram-windowing: initial release, 2022, doi:10.5281/zenodo.7034265.
[62] E. Remy, E. Thiel, Medial axis for chamfer distances: computing look-up tables and neighbourhoods in 2D or 3D, Pattern Recognit. Lett. 23 (2002) 649–661, doi:10.1016/S0167-8655(01)00141-6.
[63] A. Odgaard, H.J.G. Gundersen, Quantification of connectivity with special emphasis on 3D reconstructions, Bone 14 (1993) 173–182, doi:10.1016/8756-3282(93)90245-6.
[64] F. Hess, History of (MICRO) vascular surgery and the development of small-caliber blood vessel prostheses (with some notes on patency rates and re-endothelialization), Microsurgery 6 (1985) 59–69, doi:10.1002/micr.1920060202.
[65] B. Zhang, Y. Xu, S. Ma, L. Wang, C. Liu, W. Xu, J. Shi, W. Qiao, H. Yang, Small-diameter polyurethane vascular graft with high strength and excellent compliance, J. Mech. Behav. Biomed. Mater. 121 (2021) 104614, doi:10.1016/j.jmbbm.2021.104614.
[66] R.M. Nezarati, M.B. Eifert, D.K. Dempsey, E. Cosgriff-Hernandez, Electrospun vascular grafts with improved compliance matching to native vessels, J. Biomed. Mater. Res. - Part B Appl. Biomater. 103 (2015) 313–323, doi:10.1002/jbm.b.33201.
[67] G.C. Sieck, M. Clinic, Physiology in perspective: structure and function—anatomy and physiology are integral, Physiology 32 (2017) 264–265, doi:10.1152/physiol.00014.2017.
[68] B.B.J. Leal, N. Wakabayashi, K. Oyama, H. Kamiya, D.I. Braghirolli, P. Pranke, Vascular tissue engineering: polymers and methodologies for small caliber vascular grafts, Front. Cardiovasc. Med. 7 (2021) 1–18, doi:10.3389/fcvm.2020.592361.
[69] S. Ravi, Z. Qu, E.L. Chaikof, Polymeric materials for tissue engineering of arterial substitutes, Vascular 17 (2009) 1–15, doi:10.2310/6670.2008.00084.
[70] X. Wang, V. Chan, P.R. Corridon, Acellular tissue-engineered vascular grafts from polymers: methods, achievements, characterization, and challenges, Polymers 14 (2022) 4825, doi:10.3390/polym14224825.
[71] E.H. Stephens, K.J. Grande-Allen, Age-related changes in collagen synthesis and turnover in porcine heart valves, J. Heart Valve Dis. 16 (2007) 672–682.
[72] T. Tsuruda, A. Yamashita, M. Otsu, M. Koide, Y. Nakamichi, Y. Sekita-Hatakeyama, K. Hatakeyama, T. Funamoto, E. Chosa, Y. Asada, N. Udagawa, J. Kato, K. Kitamura, Angiotensin II induces aortic rupture and dissection in osteoprotegerin-deficient mice, J. Am. Heart Assoc. 11 (2022), doi:10.1161/JAHA.122.025336.
[73] A. Mieremet, M. van der Stoel, S. Li, E. Coskun, T. van Krimpen, S. Huveneers, V. de Waard, Endothelial dysfunction in Marfan syndrome mice is restored by resveratrol, Sci. Rep. 12 (2022) 1–12, doi:10.1038/s41598-022-26662-5.
[74] W.W. Lim, J. Dong, B. Ng, A.A. Widjaja, C. Xie, L. Su, X.Y. Kwek, N.G.Z. Tee, C. Jian Pua, S. Schafer, S. Viswanathan, S.A. Cook, Inhibition of IL11 signaling reduces aortic pathology in murine marfan syndrome, Circ. Res. 130 (2022) 728–740, doi:10.1161/CIRCRESAHA.121.320381.
[75] L.F. Borges, J.P.F. Blini, R.R. Dias, P.S. Gutierrez, Why do aortas cleave or dilate? Clues from an electronic scanning microscopy study in human ascending aortas, J. Vasc. Res. 51 (2013) 50–57, doi:10.1159/000356296.
[76] A. Ben Zemzem, X. Liang, L. Vanalderwiert, C. Bour, B. Romier-Crouzet, S. Blaise, M.J. Sherratt, T. Weitkamp, M. Dauchez, S. Baud, N. Passat, L. Debelle, S. Almagro, Early alterations of intra-mural elastic lamellae revealed by synchrotron X-ray micro-CT exploration of diabetic aortas, Int. J. Mol. Sci. 23 (2022) e21844, doi:10.3390/ijms23063250.
[77] J. Fan, T. Watanabe, Atherosclerosis: known and unknown, Pathol. Int. 72 (2022) 151–160, doi:10.1111/pin.13202.
[78] C. Dullin, R. Ufartes, E. Larsson, S. Martin, M. Lazzarini, G. Tromba, J. Missbach-Guentner, D. Pinkert-Leetsch, D.M. Katschinski, F. Alves, μCT of ex-vivo stained mouse hearts and embryos enables a precise match between 3D virtual histology, classical histology and immunochemistry, PLoS One 12 (2017), doi:10.1371/journal.pone.0170597.
[79] S.R. Sompuram, K. Vani, E. Messana, S.A. Bogen, A molecular mechanism of formalin fixation and antigen retrieval, Am. J. Clin. Pathol. 121 (2004) 190–199, doi:10.1309/BRN7CTX1E84NWWPL.
[80] C.H. Fox, C. Benton, Formaldehyde: the fixative, J. Histotechnol. 10 (1987) 199–201, doi:10.1179/his.1987.10.3.199.
[81] A.D. Meade, C. Clarke, F. Draux, G.D. Sockalingum, M. Manfait, F.M. Lyng, H.J. Byrne, Studies of chemical fixation effects in human cell lines using Raman microspectroscopy, Anal. Bioanal. Chem. 396 (2010) 1781–1791, doi:10.1007/s00216-009-3411-7.
[82] I. Eltoum, J. Fredenburgh, R.B. Myers, W.E. Grizzle, Introduction to the theory and practice of fixation of tissues, J. Histotechnol. 24 (2001) 173–190, doi:10.1179/his.2001.24.3.173.
[83] E.A. Susaki, C. Shimizu, A. Kuno, K. Tainaka, X. Li, K. Nishi, K. Morishima, H. Ono, K.L. Ode, Y. Saeki, K. Miyamichi, K. Isa, C. Yokoyama, H. Kitaura, M. Ikemura, T. Ushiku, Y. Shimizu, T. Saito, T.C. Saido, M. Fukayama, H. Onoe, K. Touhara, T. Isa, A. Kakita, M. Shibayama, H.R. Ueda, Versatile whole-organ/body staining and imaging based on electrolyte-gel properties of biological tissues, Nat. Commun. 11 (2020) 1982, doi:10.1038/s41467-020-15906-5.
[84] K. Stroobants, V. Goovaerts, G. Absillis, G. Bruylants, E. Moelants, P. Proost, T.N. Parac-Vogt, Molecular origin of the hydrolytic activity and fixed regioselectivity of a ZrIV-substituted polyoxotungstate as artificial protease, Chem. - A Eur. J. 20 (2014) 9567–9577, doi:10.1002/chem.201402683.
[85] E. Gasteiger, C. Hoogland, A. Gattiker, S. Duvaud, M.R. Wilkins, R.D. Appel, A. Bairoch, in: The Proteomics Protocols Handbook, Hamana press, 2005, pp. 571–608, doi:10.1385/1592598900.